

1

2     **A Field Study of Pixel-Scale Variability of Raindrop Size Distribution in the**

3                         **Mid-Atlantic Region**

4

5                         *Ali Tokay\**

6     *Joint Center For Earth Systems Technology, University of Maryland Baltimore County*

7                         *and NASA Goddard Space Flight Center, Greenbelt, Maryland*

8                         *Leo Pio D'Adderio*

9     *Department of Physics and Earth Science, The University of Ferrara, Ferrara, Italy*

10                         *David B. Wolff and Walter A. Petersen*

11     *NASA Goddard Space Flight Center, Wallops Flight Facility, Wallops Island, Virginia*

12

13                         *Submitted to Journal of Hydrometeorology*

14                         *August 13, 2015*

15

16

17

18

19     \* Corresponding author's address:

20     NASA Goddard Space Flight Center, Code 612.0

21     Greenbelt, MD 20771

22     tokay@umbc.edu

23

24

## Abstract

25

26 The spatial variability of parameters of raindrop size distribution and its derivatives  
27 is investigated through a field study where collocated PARSIVEL<sup>2</sup> and two-  
28 dimensional video disdrometers are operated at six sites in Wallops Island, Virginia  
29 from December 2013 to March 2014. The three-parameter exponential function is  
30 employed to determine the spatial variability across the study domain where the  
31 maximum separation distance was 2.3 km. The nugget parameter of exponential  
32 function is set to 0.99 and the correlation distance ( $d_0$ ) and shape parameter ( $s_0$ ) are  
33 retrieved minimizing root-mean-square error, after fitting it to the correlations of  
34 physical parameters. Fits were very good for almost all fifteen physical parameters.  
35 The retrieved  $d_0$  and  $s_0$  were about 4.5 km and 1.1, respectively, for rain rate (RR)  
36 when all twelve disdrometers were reporting rainfall with a rain rate threshold of  
37 0.1 mm h<sup>-1</sup> in one-minute observations. The  $d_0$  decreased noticeably when one or  
38 more disdrometers were required to report rain. The  $d_0$  was considerably different  
39 for a number of parameters (e.g. mass weighted diameter) but was about the same  
40 for the other parameters (e.g. RR) when rainfall threshold was reset to 12 dB for Ka-  
41 band and 18 dB for Ku-band reflectivity following the expected Global Precipitation  
42 Measurement mission's space-borne radar minimum detectable signals. The  
43 reduction of the database through elimination of a site did not alter  $d_0$  as long as the  
44 fit was adequate. The correlations of 5-minute rain accumulations were lower when  
45 disdrometer observations were simulated for a rain gauge at different bucket sizes.

46

47 1. Introduction

48

49 The National Aeronautics and Space Administration (NASA) Global Precipitation  
50 Measurement (GPM) mission aims to retrieve the three dimensional hydrometeor  
51 size distribution of precipitation through its Dual-frequency Precipitation Radar  
52 (DPR) on board the GPM core satellite (Hou et. al. 2014). The retrieval algorithm  
53 outputs parameters of gamma model size distribution for each range bin utilizing  
54 Ka- and Ku-band radar measurements (Seto et al. 2013). The lowest clutter free  
55 range bin near the surface at nadir incidence is approximately 5 km radius and 125  
56 m height. One of the key uncertainties of retrieved size distributions is its spatial  
57 variability within a given DPR footprint. The spatial variability is a result of  
58 precipitation gradient within the range volume, which may not be completely  
59 covered by the precipitation. This variability contributes to Non-Uniform Beam  
60 Filling (NUBF) which results in a higher degree of uncertainty in microwave sensor  
61 based precipitation estimates where the instantaneous field of view is typically  
62 bigger than the DPR footprint (Tokay et al. 2014a).

63

64 Scanning radars in range height indicator mode provides the most relevant data  
65 source to study the spatial variability of hydrometeor size distribution in the  
66 vertical, while gridded radar data at 1x1 km or 2x2 km resolution is a common  
67 resource for studying the horizontal spatial variability. The parameters of the size  
68 distribution that are derived from radar measurements are based on empirical  
69 relationships (Bringi et al. 2004). There is also an uncertainty within the radar pixel

70 as its size increases away from radar. Disdrometers are an alternative resource for  
71 estimating the horizontal spatial variability but are associated with point sampling  
72 and it is quite costly to populate a dense network with disdrometers to sample the  
73 area of a satellite footprint. Therefore, there have been relatively few field studies  
74 conducted to determine the spatial variability of hydrometeor size distributions and  
75 all of these dealt with rainfall.

76

77 As part of the NASA's Tropical Rainfall Measurement Mission (TRMM) Ground  
78 Validation program, a number of impact type Joss-Waldvogel disdrometers were  
79 first deployed during a series of field campaigns and also deployed later at the NASA  
80 Wallops Flight Facility on Wallops Island, Virginia. The latter operation allowed for  
81 determination of the measurement accuracy of the disdrometers when six units  
82 were side-by-side (Tokay et al. 2005) and the spatial variability of raindrop size  
83 distribution (DSD) when three units were deployed across the Wallops Island strip,  
84 where the minimum and maximum separation distances were 0.65 and 1.7 km,  
85 respectively (Tokay and Bashor 2010). Later, four disdrometers were distributed  
86 across the same strip where the minimum and maximum separation distances were  
87 0.4 and 5.0 km, respectively (Schröer 2011). The three-parameter exponential  
88 function was tested to determine the spatial variability of DSD and integral rain  
89 parameters. Since four disdrometers provide six pairs of correlations across 5 km,  
90 the fitted exponential function was subject to noticeable error.

91

92 Measurement accuracy is one of the key uncertainties in determining the spatial  
93 variability of DSDs quantitatively. Each disdrometer type has its own shortcomings  
94 in measuring the DSD, and comparative field studies where different types of  
95 disdrometers were collocated, help quantify the uncertainties of the disdrometers  
96 (Krajewski et al. 2006, Thurai et al. 2011, Tokay et al. 2013, 2014b). Indeed, the  
97 Miriovsky et al. (2004) pioneer study was unable to determine the spatial variability  
98 of reflectivity within 1 km<sup>2</sup> due to uncertainties of four different types of  
99 disdrometers. Lee et al. (2009), on the other hand, used four Particle Occurrence  
100 Sensor System (POSS) to study the spatial variability of DSD in stratiform rain  
101 events. An S-band dual polarization radar scanned over the POSS units and the  
102 spatial correlation of rainfall was higher in radar than in POSS especially at 15 and  
103 30 km. This could partly be due to the differences between the sampling volumes of  
104 the instruments.

105

106 The first comprehensive field study to quantify the spatial variability of the DSD was  
107 conducted in Central Spain where eight dual PARSIVEL (PARticle Size VELOCITY)  
108 disdrometers were deployed (Tapiador et al. 2010). The availability of number of  
109 disdrometers allowed 28 pairs of correlations where the distances range from 0.2  
110 km to 3.2 km. The dual units were aligned in both North-South and East-West  
111 directions, and one of the five events had significant differences in correlations of  
112 reflectivity between North-South and East-West aligned disdrometers. Jaffrain et al.  
113 (2011), on the other hand, analyzed 53 hours of 16 PARSIVEL observations to  
114 determine the spatial variability of DSD in a radar pixel (about 1 x 1 km<sup>2</sup>) in

115 Lausanne, Switzerland. They concluded that the coefficient of variations for the  
116 mass weighted diameter ( $D_{\text{mass}}$ ), total concentration ( $N_T$ ), and rain rate (RR) were  
117 high and could not be explained solely by the uncertainty of the measurement.  
118 Jaffrain and Berne (2012, JB12 hereafter) used the same set up of instruments to  
119 determine the spatial variability of  $D_{\text{mass}}$ ,  $N_T$ , and RR using a variogram analysis.  
120 They reported that the variability was greater in convective rain than transitional  
121 and frontal rain. They also noted a decreasing variability with decreasing temporal  
122 resolution. Perhaps, the main issue of these studies is the measurement accuracy of  
123 the PARSIVEL disdrometer. The low-cost laser resulted in overestimation of large  
124 drops due to an inhomogeneous beam (Thurai et al. 2011, Tokay et al. 2013). The  
125 manufacturer upgraded the PARSIVEL disdrometer with PARSIVEL<sup>2</sup> in 2011 (Tokay  
126 et al. 2014b).

127

128 In contrast to disdrometers, rain gauges are low-cost, durable, easy to maintain and  
129 are frequently deployed to adjust or validate radar rainfall estimates during either  
130 two-month long field studies or longer-term field observations. Thus, rain gauge  
131 networks are an excellent resource to study the spatial variability of rainfall (Habib  
132 and Krajewski 2002, Gebremichael and Krajewski 2004, Ciach and Krajewski 2006,  
133 among others). The spatial variability of rainfall is often quantified applying a three-  
134 parameter exponential function to the corrections between the paired gauge  
135 measurements. The parameters of the exponential function differs from one study  
136 to another due to the differences in quality of rain gauge data, inter-gauge distances,  
137 sample size, experiment period and location (Villarini et al. 2008). Logistics may

138 limit the inter-gauge distances, while long-term observations with dual or multiple  
139 gauge at each site has a clear advantage for a larger sample size and continuous  
140 gauge record at a given gauge site. The long-term observations also allow  
141 investigation of season-to-season differences in the spatial variability of rainfall.  
142 Tokay et al. (2014a), for instance, used five years of continuous rain gauge  
143 measurements in the Southern Delmarva Peninsula and showed that weather  
144 systems dominate spatial variability over a season. Nor'easters, for instance,  
145 dominate winter precipitation in the Mid-Atlantic region.

146

147 As a comparative study, the spatial variability of rainfall was quantified through X-  
148 band radar and rain gauge network (Moreau et al. 2009). The correlations between  
149 the paired radar pixels at 1 km<sup>2</sup> resolution were significantly higher than those  
150 between paired gauges underneath the radar pixel up to 8 km. The differences in  
151 correlations are attributed to the differences in sampling volume, while the errors in  
152 radar rainfall estimate and time-height ambiguity also be played a role. Another  
153 comparative study of the spatial variability of rainfall was conducted using S-band  
154 dual-polarization radar and 2DVD measurements during Mid-latitude Continental  
155 Convective Clouds Experiment (MC3E) (Bringi et al. 2015). A good agreement was  
156 found between the radar and disdrometer based spatial variability for RR, median  
157 volume diameter, and logarithmic normalized intercept parameter with respect to  
158 liquid water content (N<sub>w</sub>) in a long lasting stratiform event. The correlation  
159 distances were lower in a relatively short convective event than the stratiform event  
160 for all three parameters.

161  
162 This study investigates the pixel-space variability of DSD and integral rain  
163 parameters employing a disdrometer network at NASA Wallops Flight Facility  
164 (WFF), Wallops Island, Virginia (37.9 degree N and 75.4 degree W). The manuscript  
165 is organized as follows: The disdrometer network and the database are presented in  
166 Section 2. Section 3 introduces the three-parameter exponential function while the  
167 parametric form of the DSD is given in Section 4. The probability and cumulative  
168 distributions of the DSD and rain parameters can be found in Section 5. Section 6  
169 depicts the spatial variability of DSD and rain parameters, while the sensitivity  
170 studies are in Section 7. The conclusions are given in the last section.

171

172 2. Field Study

173

174 The disdrometer network consists of six sites where each site had one two  
175 dimensional video disdrometer (2DVD) and one PARASIVE<sup>2</sup> disdrometer. The sites  
176 were distributed across WFF where the minimum and maximum separation  
177 distances were 0.5 and 2.3 km, respectively (Figure 1a). One of the sites (Pad)  
178 hosted a variety of tipping and weighing bucket rain gauges including two pit gauges  
179 (Figure 1b). Another site was collocated with the Wallops Automated Surface  
180 Observing System (ASOS) as well as additional tipping bucket rain gauges (Figure  
181 1c). Table 1 summarizes the locations and distances between the sites.

182

183 PARSIVEL<sup>2</sup> is the third generation of the laser-optical PARSIVEL disdrometer  
184 (Tokay et al. 2014b). It is designed to measure the size and fall velocity of individual  
185 hydrometeors across its laser beam and is also present weather sensor. For rain,  
186 PARSIVEL outputs drop counts in a 32 x 32 size versus fall velocity matrix at  
187 selected time intervals ranging from 10-second to one-minute. The first two size  
188 bins are empty due to low signal to noise ratio and the smallest measurable  
189 raindrop corresponds to 0.25 mm diameter. The width of the size bins increases  
190 with the size of raindrops from 0.125 mm for drops to 1.2 mm, to 0.25 for drops up  
191 to 2.5 mm, to 0.5 mm for drops up to 5 mm, and to 1.0 mm for the larger drops.  
192 Therefore, there is noticeable uncertainty in determining the maximum drop size of  
193 the DSD. Based on 2DVD observations, the largest raindrop ever recorded is 9.7 mm  
194 diameter (Gatlin et al. 2015). The 25<sup>th</sup> bin corresponds to 9-10 mm and was  
195 considered as the largest bin for rain. For fall velocity, PARSIVEL has a range from  
196 0.05 to 20.8 m s<sup>-1</sup>, covering fall speeds of all types of hydrometeors. For rain, the  
197 26<sup>th</sup> bin corresponds to 8-9.6 m s<sup>-1</sup>, and covers the expected range for terminal fall  
198 speeds of very large raindrops (Beard 1976). However, PARSIVEL<sup>2</sup> underestimates  
199 the fall velocity of raindrops by approximately 1 m s<sup>-1</sup> with respect to the expected  
200 terminal fall speed of raindrops at around 1 mm diameter (Tokay et al. 2014b). The  
201 underestimation in fall velocity is also evident for larger drops but the difference  
202 between the mean PARSIVEL<sup>2</sup> and terminal fall speed decreases with increasing size.  
203 The manufacturer recognizes this matter as a software error and it is expected that  
204 the new generation of instruments will mitigate this issue (Kurt Nemeth, OTT  
205 PARSIVEL, *personal communication*, 2015).

206

207 The 2DVDs are the “compact” third generation and are composing of sensor unit and  
208 indoor personal computer (Schönhuber et al. 2007). The third generation compact  
209 version has the optical components firmly mounted with no need for re-alignment  
210 by the user. The distance of the optical slits to the rim of the housing was also  
211 reduced aiming to eliminate inhomogeneous filling of the measurement area in  
212 windy conditions. The high-speed line-scan cameras provides better matching of  
213 falling hydrometeors between the two planes that are nominally 6 mm apart. The  
214 2DVD records the time stamp of each raindrop including its equivalent diameter, fall  
215 velocity, and oblateness as well as the sampling area. Common interruption of data  
216 occurs often due to non-meteorological items (e.g. leaves) in the sampling cross  
217 section, which is the main shortcoming of the 2DVD.

218

219 The dataset for this study spanned from December 2013 through March 2014.  
220 While PARSIVEL<sup>2</sup> disdrometers operated nearly continuous during the experiment  
221 period, a number of 2DVD units failed to operate in a few rain events. The raw  
222 outputs of PARSIVEL<sup>2</sup> and 2DVD observations were integrated to one-minute after  
223 screening secondary and mismatched drops that fell outside  $\pm 50\%$  of their terminal  
224 fall speed (Tokay et al. 2013). Several rain/no-rain thresholds were then applied to  
225 the one-minute observations. All thresholds required a minimum of 10 drops. The  
226 minimum RR of 0.1 mm h<sup>-1</sup> resulted in 447 one-minute samples when all twelve  
227 disdrometers reported rainfall. Considering the minimum detectable reflectivity of  
228 the GPM DPR, the Ku-band reflectivity ( $Z_{Ku}$ ) of 18 dB and Ka-band reflectivity ( $Z_{Ka}$ )

229 of 12 dB (Seto et al. 2013) are the other two thresholds used in this study. The  
230 minimum RR was 0.11 and 0.08 mm h<sup>-1</sup> for Z<sub>Ka</sub> > 12 dB and 0.16 and 0.30 mm h<sup>-1</sup> for  
231 Z<sub>Ku</sub> > 18 dB for 2DVD and PARASVEL<sup>2</sup>, respectively. The sample sizes were 445 and  
232 278 for Z<sub>Ka</sub> > 12 dB and Z<sub>Ku</sub> > 18 dB, respectively. The sample of Z<sub>Ka</sub> > 12 included  
233 twelve one-minute spectra that were not in the RR > 0.1 mm h<sup>-1</sup> based sample.

234

235 3. Methodology

236

237 A three-parameter exponential function is employed to quantify the spatial  
238 variability of the DSD. It has been widely used to determine the spatial variability of  
239 rainfall through rain gauge and radar rainfall studies (Habib and Krajewski 2002,  
240 Gebremichael and Krajewski 2004, Ciach and Krajewski 2006, Villarini et al. 2008,  
241 Moreau et al. 2009, Tokay et al. 2014a). The Pearson correlation coefficient, r, is  
242 applied to the selected DSD and rain parameters that are derived from disdrometer  
243 measurements at distance d. The parametric form of exponential function is then  
244 expressed as

245

$$246 \quad r = r_0 \exp\left(-\frac{d}{d_0}\right)^{s_0} \quad (1)$$

247

248 where r<sub>0</sub> is the correlation of a selected parameter derived from collocated  
249 instruments and is known as the nugget parameter and ideally should be one.  
250 However, collocated gauge and disdrometer observations show that the nugget

251 parameter ranges between 0.90 and 0.99. The other parameters of the exponential  
252 function are not sensitive to changes in  $r_0$  within this range (Schröer 2011, Tokay  
253 and Özturk, 2012). In this study,  $r_0$  was set to 0.99. The correlation distance  $d_0$ , and  
254 the shape parameter  $s_0$ , are then derived through minimizing the root mean square  
255 error between the observed and derived correlations. As an initial guess,  $d_0$  values  
256 of 1 to 300 km and  $s_0$  values of 0.1 to 2.0 were given.

257

258 The  $d_0$  decreases with increasing  $s_0$  when the correlation coefficient is high (Figure  
259 2). When the variability is investigated over a relatively small domain as in this  
260 study, the correlations of the selected DSD or rain parameters may not have a  
261 decreasing trend with distance. If the correlations were high, the best fit results in  
262 very high  $d_0$  and this should not be interpreted independent of other exponential  
263 function parameters. The parameters of exponential function are valid within the  
264 maximum distance of the study domain (Tokay and Öztürk 2012).

265

#### 266 4. Raindrop Size Distribution

267

268 The normalized gamma distribution function is adopted to determine the spatial  
269 variability of DSD parameters. The normalization was done with respect to  $N_T$  and  
270 liquid water content  $W$  (Tokay and Bashor 2010). The normalized intercept  
271 parameters with respect to total concentration,  $N_T^*$  and liquid water content,  $N_w$  are  
272 expressed as

273

274  $N_T^* = \frac{N_T}{D_{\text{mass}}}$  (2)

275

276  $N_w = \frac{256}{\pi \rho_w} \frac{10^3 W}{D_{\text{mass}}^4}$  (3)

277

278 where  $\rho_w$  is the density of water.  $D_{\text{mass}}$  is related to the slope,  $\Lambda$  and shape  
279 parameter,  $m$  of the complete gamma distribution as;

280

281  $D_{\text{mass}} = \frac{4 + m}{\Lambda}$  (4)

282

283 The normalized intercept parameters can then be calculated from observed spectra  
284 as well. The corresponding normalized gamma fitted distributions are expressed as:

285

286  $N(D) = N_T^* f_1(m) \left( \frac{D}{D_{\text{mass}}} \right)^m \exp[-(4 + m) \frac{D}{D_{\text{mass}}}]$  (5)

287

288  $N(D) = N_w f_2(m) \left( \frac{D}{D_{\text{mass}}} \right)^m \exp[-(4 + m) \frac{D}{D_{\text{mass}}}]$  (6)

289

290 where  $f_1(m)$  and  $f_2(m)$  are given as;

291

292  $f_1(m) = \frac{(4 + m)^{m+1}}{\Gamma(m + 1)}$  (7)

293

294      
$$f_2(m) = \frac{6}{256} \frac{(4+m)^{m+4}}{\Gamma(m+4)}$$
 (8)

295

296      To extract the shape parameter,  $m(N_T^*)$ , and  $m(N_W)$ , the rain rates that are calculated  
297      from observed and fitted gamma distributions (e.g. equations 5 and 6) are  
298      minimized. The formulations presented above follows the complete gamma  
299      function where minimum and maximum drop size is assumed zero and infinity,  
300      respectively. In reality, there is a minimum and maximum drop size ( $D_{max}$ ) in a  
301      population of drops and the incomplete gamma function is more appropriate  
302      especially if the size spectra do not contain the large drops (e.g. narrow  
303      distribution), but this is beyond the scope of this study.

304

305      The GPM DPR algorithm has adopted the normalized gamma function as in equation  
306      6 (Seto et al. 2013). Since the DPR algorithm employs dual frequency reflectivity  
307      measurements to determine the three parameters of gamma function, there is an  
308      interest in finding relations between the derived parameters. Williams et al. (2014)  
309      suggested a power law relation between the standard deviation of  $D_{mass}$  ( $\sigma_{mass}$ ) and  
310       $D_{mass}$ . Both variables are directly calculated from observed DSD and their ratio is a  
311      sole function of shape parameter,  $m(\sigma_{mass})$  following complete gamma function.

312

313      
$$\frac{\sigma_{mass}}{D_{mass}} = \frac{1}{(4+m)^{0.5}}$$
 (9)

314

315

316 5. Probability and Cumulative Distributions

317

318 This study investigates the spatial variability of seven DSD and eight integral rain  
319 parameters. The DSD parameters include  $D_{\text{mass}}$ ,  $D_{\text{max}}$ ,  $N_T^*$ ,  $N_w$ ,  $m(N_T^*)$ ,  $m(N_w)$ , and  
320  $m(\sigma_{\text{mass}})$ , while the rain parameters were  $W$ ,  $RR$ , dual polarization parameters of  
321 horizontal reflectivity ( $Z_H$ ), and differential reflectivity ( $Z_{\text{dr}}$ ), reflectivity at W-band  
322 ( $Z_w$ ),  $Z_{\text{Ku}}$ ,  $Z_{\text{Ka}}$ , and dual frequency ratio ( $\text{DFR} = Z_{\text{Ku}}/Z_{\text{Ka}}$ ). The Ka-, Ku-, and W-band  
323 reflectivities are calculated using Mie scattering for spherical particles, while dual-  
324 polarization parameters are calculated for S-band radar following Tokay et al.  
325 (2002). Table 2 presents the mean, standard deviation, median, and 5<sup>th</sup> and 95<sup>th</sup>  
326 percentage of 15 physical parameters. Both  $N_T^*$  and  $N_w$  have ranges of several order  
327 of magnitude and, hence logarithmic values of these two parameters are used in  
328 constructing probability and cumulative distributions.

329

330 Among many factors listed in the introduction, knowledge of the characteristics of  
331 the DSD and rainfall is essential for quantifying the spatial variability. Observed  
332 DSD lacking large drops but with abundant small drops will incur different spatial  
333 variability than a DSD with numerous large drops but fewer small drops. The  
334 spatial variability of rainfall, on the other hand, differs in the presence and absence  
335 of heavy rain. The probability and cumulative distributions of the DSD and rain  
336 parameters provide an insight on the characteristics of DSD and rainfall, and these

337 distributions should be included if a similar study is conducted with a different  
338 dataset.

339

340 Figure 3 presents the probability and cumulative distributions of fifteen DSD and  
341 integral rain parameters based on 2DVD and PARSIVEL<sup>2</sup> measurements, when all  
342 twelve units were reporting rainfall. A very good agreement in midsize range  
343 (diameter 1-3 mm) of 2DVD and PARSIVEL<sup>2</sup> size spectra reflects an excellent  
344 agreement in probability and cumulative distributions of  $D_{\text{mass}}$  between the two  
345 disdrometers (Figure 2a).  $D_{\text{mass}}$  mostly resided between 0.8 and 1.5 mm, peaking at  
346 1 mm (Table 2). The binning of drop counts results in quantization error in size  
347 measurements in PARSIVEL<sup>2</sup>, which is quite significant for  $D_{\text{max}}$  since the larger bins  
348 have wider widths. The probability distribution of  $D_{\text{max}}$  in PARSIVEL<sup>2</sup> therefore had  
349 multiple modes, while the probability distribution of  $D_{\text{max}}$  in 2DVD was a unimodal  
350 (Figure 3b). The cumulative distributions of  $D_{\text{max}}$  agreed well between the two  
351 types of disdrometers and the median  $D_{\text{max}}$  was around 1.9 mm for both (Table 2).

352

353 PARSIVEL<sup>2</sup> is relatively more sensitive to small drops less than 0.5 mm diameter  
354 than the 2DVD (Tokay et al. 2013, 2014b).  $N_T^*$  is very sensitive to the number of  
355 small drops since their concentrations are much higher than larger drops. The  
356 probability distribution of  $\log(N_T^*)$  of 2DVD and PARSIVEL<sup>2</sup> show a wide range, but  
357 the PARSIVEL<sup>2</sup> based distribution was shifted to the larger concentrations,  
358 consistent with its sensitivity to small drops (Figure 3c).  $N_w$  is more sensitive to  
359 midsize drops and therefore an agreement is expected between the 2DVD and

360 PARSIVEL<sup>2</sup> distributions. A general agreement is evident between the distributions  
361 of log( $N_w$ ) with a median 3.55, but the PARSIVEL<sup>2</sup> also had low percentages of  
362 log( $N_w$ ) less than 2.5 (Figure 3d).

363

364 The shape parameter of the gamma distribution is very sensitive to the method of  
365 derivation and has a wide range but was mostly between 0 and 14 with mean and  
366 median around 5 (Table 2). While the agreement between 2DVD and PARSIVEL<sup>2</sup>  
367 derived distributions of shape parameters were reasonable for  $m(N_t^*)$   $m(N_w)$ , and  
368  $m(\sigma_{mass})$ , the probability distribution of  $m(N_t^*)$  was shifted toward larger values in  
369 PARSIVEL<sup>2</sup> and  $m(N_w)$  and  $m(\sigma_{mass})$  had slightly larger values in 2DVD (Figures 3e-  
370 g). The differences in probability and cumulative distributions are more  
371 pronounced in  $m(N_t^*)$  reflecting the differences in distributions of log( $N_t^*$ ).

372

373 An excellent agreement was evident in the distributions of W, and RR between the  
374 two different types of disdrometers (Figures 3h-i). Both W and RR are primarily  
375 sensitive to midsize drops, while the upper end of the small drops (0.8-1.0 mm) and  
376 the lower end of the large drops (3.0-4.0 mm) contribute to W and RR significantly  
377 in the presence of light and heavy rainfall, respectively. The mean and median RR is  
378 1.1 and 0.9 mm h<sup>-1</sup>, respectively (Table 2), indicating the dominance of light rain.  
379 Good agreement was also evident in distributions of Z<sub>H</sub>, Z<sub>dr</sub>, Z<sub>W</sub>, Z<sub>Ku</sub>, Z<sub>Ka</sub>, and DFR  
380 between the two types of disdrometers (Figures 3j-o). The median Z<sub>H</sub>, Z<sub>Ku</sub> and Z<sub>Ka</sub>  
381 were in the 22-23 dB range, while 95<sup>th</sup> percentiles were in the 31-32 dB range  
382 (Table 2) in the presence of widespread frontal rainfall.

383

384 6. Spatial Variability

385

386 The correlations of  $D_{\text{mass}}$  and  $D_{\text{max}}$  are higher for 2DVD than for PARSIVEL<sup>2</sup> at a given  
387 distance (Figures 4a-b). PARSIVEL<sup>2</sup> based correlations were 0.55-0.7 for five paired  
388 observations resulting in a higher RMSE. The quantization error due to binning  
389 contributed to the low correlations in PARSIVEL<sup>2</sup> based  $D_{\text{max}}$ . The correlations of  
390  $N_T^*$  and  $N_w$  were higher than 0.9 for all distances for the 2DVD and decreased  
391 gradually with distance (Figures 4c-d). PARSIVEL<sup>2</sup> based correlations have a wider  
392 range than 0.1 at a given distance but remained higher than 0.84 and the RMSE was  
393 quite low for fitted exponential function. The correlations of shape parameters  
394 decreased with distance from 0.8 to 0.5 for  $m(N_T^*)$  and from 0.8 to 0.4 for  $m(N_w)$   
395 and  $m(\sigma_{\text{mass}})$  for both 2DVD and PARSIVEL<sup>2</sup> (Figures 4e-g). The range of  
396 correlations was less than 0.1 at a given distance for both disdrometers resulting in  
397 low RMSE. The sample size was 74% and 77% of the database for  $m(N_T^*)$  and  
398  $m(N_w)$ , respectively due to the fact that the shape parameter was outside the  
399 expected range of -4 to 20 for a number of size spectrum when normalized gamma  
400 function was fitted minimizing rain rate. Similarly, the sample size was 76% of the  
401 database for  $m(\sigma_{\text{mass}})$  due to presence of shape parameters larger than 20. The  
402 large shape parameters results from narrow size spectrum in the absence of large  
403 drops. The shape of size spectrum exhibits more than a single peak with a plateau  
404 in midsize regime for collisional break-up dominated DSD (D'Adderio et al. 2015).

405 The gamma distribution is not the best mathematical fit in these conditions, but this  
406 is beyond scope of this paper.

407

408 The correlations of RR and W decreased with distance from 0.9 to 0.55 and from  
409 0.92 to 0.64, respectively (Figures 4h-i). The spread in correlation between the  
410 same and different types of disdrometers was much less than 0.1 at a given distance  
411 resulting in very low RMSE. Thus, the exponential fits were nearly identical for both  
412 types of disdrometers. The correlations of reflectivities at different wavelengths  
413 decreased with distance but there were noticeable differences and similarities  
414 among them. The correlations of  $Z_H$  and  $Z_{Ku}$  were about the same at a given distance  
415 for a given disdrometer while the spread in PARSIVEL<sup>2</sup> derived correlations of  $Z_{Ka}$   
416 were less resulting in lower RMSE (Figures 4j, 4m-n). The spread in correlations of  
417  $Z_W$  were much less (less than 0.05) at a given distance for both disdrometer types  
418 resulting in an excellent fit (Figure 4l). For  $Z_{dr}$ , there were significantly lower  
419 correlations (0.35-0.55) for five PARSIVEL<sup>2</sup> pairs resulting in high RMSE (0.14)  
420 (Figure 4k). For 2DVD,  $Z_{dr}$  decreased with distance and had a spread of 0.1 at a given  
421 distance resulting in a reasonable fit with low RMSE. DFR, which is another  
422 reflectivity ratio, had lower correlations even at short distances and the spread in  
423 correlations were as high as 0.3 at a given distance in PARSIVEL<sup>2</sup> resulting in  
424 relatively poor fit with high RMSE (0.12) (Figure 4o). For 2DVD, the fit was better  
425 but the spread in correlation was 0.2 at a given distance.

426

427 The correlation distances were about the same for RR and W but higher in 2DVD  
428 than in PARSIVEL<sup>2</sup> for the rest of rain and DSD parameters (Figure 5a). For  $N_T^*$  and  
429  $N_w$ ,  $d_0$  was at around upper limit of initial guess due to high correlations for all  
430 distances. The  $d_0$  was 4.2 and 4.5 km in RR in PARSIVEL<sup>2</sup> and 2DVD, respectively.  
431 These correlation distances correspond to high spatial variability following gauge-  
432 based studies (Ciach and Krajewski 2006). However, the correlations remained  
433 high ( $> 0.7$ ) in this study (Figure 4i). The gauge studies were conducted for 5-  
434 minute or longer integration periods while high temporal scale in this study results  
435 in higher variability even in the presence of lighter rain. The shape parameter, on  
436 the other hand, remained between 0.4 and 1.0 for most of the fits (Figure 5b). The  
437 RMSE was less than 0.08 for almost all parameters showing the goodness of fit  
438 (Figure 5c). It should be emphasized that three-parameter exponential function is  
439 applied for the first time for a number of DSD and rain parameters following  
440 feasibility study (Schröer 2011). Therefore, there is no direct comparison available  
441 for these parameters of exponential function with any other studies.

442

443 7. Sensitivity Studies

444

445 a) Disdrometer network availability

446

447 It is not uncommon that one or more disdrometers fail to operate throughout a field  
448 campaign. For spatial variability, it is important to assess the goodness of fit of the  
449 three-parameter exponential function when one of the sites is not available. In that

450 regard, five out of six sites were employed to quantify the sensitivity of parameters  
451 of exponential function to  $D_{\text{mass}}$  and RR. The elimination of a site reduced paired  
452 correlations from 15 to 10 and if site 5 or site 6 in Table 1 were not functioning, the  
453 maximum separation distance would be reduced to 1.84 km.

454

455 Fits were very good for 2DVD derived  $D_{\text{mass}}$  and RR regardless of the choice of  
456 elimination of paired correlations. The  $d_0$  had a very narrow range of 4.2-4.7 km for  
457 RR but remained mostly within 11-21 km for  $D_{\text{mass}}$  (Figure 6a). For PARSIVEL<sup>2</sup>, fits  
458 were good for RR but quite poor for  $D_{\text{mass}}$  repeating previous finding in Figure 4a.  
459 The  $d_0$  had a wide range in PARSIVEL<sup>2</sup> derived  $D_{\text{mass}}$  but was not sensitive to the  
460 elimination of any paired correlation in RR. The  $s_0$  was less than 1.0 and highly  
461 variable due to elimination of paired correlation in  $D_{\text{mass}}$  but remained mostly above  
462 1.0 with almost no sensitivity to the elimination of paired correlation in RR (Figure  
463 6b). The RMSE was 0.03 or less for 2DVD for both  $D_{\text{mass}}$  and RR but was higher than  
464 0.1 for four trials for PARSIVEL<sup>2</sup> derived  $D_{\text{mass}}$  (Figure 6c).

465

466 b) Rain/No-rain threshold

467

468 The rain/no-rain threshold results in differences in the sample size and the  
469 distribution of the DSD and rain parameters. The higher sensitivity DPR footprint  
470 where  $Z_{\text{Ka}}$  is larger than 12 dB is expected to have less spatial variability with higher  
471  $d_0$  than the lower sensitivity DPR footprint where  $Z_{\text{Ku}}$  is larger than 18 dB. As shown  
472 in the gauge based study of Tokay and Özturk (2012), the higher thresholds

473 eliminate the light rain or low reflectivity samples and results in lower correlations,  
474 especially if there is no precondition where both disdrometers must report rainfall.

475

476 Based on 2DVD observations,  $d_0$  of  $D_{\text{mass}}$  was the lowest and the highest for  $Z_{\text{Ku}}$  and  
477 RR thresholds, respectively (Figure 7a). The  $d_0$  of RR and W was the same for RR  
478 and  $Z_{\text{Ka}}$  thresholds and slightly lower for  $Z_{\text{Ku}}$  threshold. The  $d_0$  of  $Z_{\text{Ka}}$ ,  $Z_{\text{Ku}}$ , and  $Z_{\text{H}}$   
479 were about the same for  $Z_{\text{Ka}}$  and  $Z_{\text{Ku}}$  thresholds, and were lower than RR threshold.  
480 The  $d_0$  of DFR was the same for all three thresholds, while the other DSD and rain  
481 parameters showed different trends. The shape parameter of exponential function  
482 showed little or no variability when  $d_0$  was about the same for given thresholds  
483 (Figure 7b). The RMSE did not show significant differences between the different  
484 thresholds for most of the DSD and rain parameters except for  $Z_{\text{dr}}$  and DFR where  
485 RMSE was noticeably higher for  $Z_{\text{Ku}}$  threshold (Figure 7c).

486

487 c) Rain coverage

488

489 Partial coverage of satellite footprint or radar pixel by rain is one of the sources of  
490 NUBF and contributes significantly to the spatial variability. To quantify the spatial  
491 variability in the presence of partial coverage, PARSIVEL<sup>2</sup> observations were  
492 reprocessed when all units were reporting rainfall and when at least one unit  
493 reporting rainfall. The latter is more commonly observed in nature. The sample  
494 size is 4,645 one-minute size distributions for the latter condition, which makes it  
495 more than 2.6 times of the sample size of the former condition. The difference is

496 mainly due to the rain intermittence. The sample size when all six PARSIVEL<sup>2</sup>  
497 reported rainfall was 4 times larger than that when all twelve disdrometers  
498 reported rainfall.

499

500 The correlation distance was distinctly lower for almost all physical parameters  
501 when one or more PARSIVEL<sup>2</sup> reported rainfall (Figure 8a). It should also be noted  
502 that  $d_0$  was different from earlier findings when all six PARSIVEL<sup>2</sup> were reporting  
503 rainfall. The bigger sample included more uniform rainfall across the study domain  
504 and  $d_0$  of RR was 14 km. The  $s_0$  was higher when one or more PARSIVEL<sup>2</sup> reported  
505 rainfall (Figure 8b). Fits were good for both conditions for physical parameters  
506 except for normalized intercept and shape parameter of the gamma distribution  
507 where fit was relatively poor with RMSE of 0.1 or higher (Figure 8c).

508

509 d) Rain gauge simulation

510

511 Tipping bucket rain gauges are widely used in precipitation studies but suffer from  
512 significant sampling errors over short integration periods depending on the bucket  
513 size (Habib et al 2001). A bucket size of 0.01 inch (0.254 mm) is used in ASOS  
514 network but the gauge manufacturers also provide gauges with bucket resolutions  
515 of 0.1 mm and 0.2 mm. The gauge based spatial variability of rainfall studies  
516 employs 5-minute or longer integration periods to mitigate the sampling errors.

517

518 PARSIVEL<sup>2</sup> and 2DVD one-minute rain rate time series were employed to simulate  
519 the time of tip for 0.1 mm, 0.2 mm, and 0.254 mm bucket resolutions. The  
520 simulation study ignored any disdrometer malfunctions throughout the experiment  
521 period. The 5-minute rainfall was then calculated from one-minute disdrometer  
522 and three different simulated gauge datasets. The nugget parameter of 0.99 was  
523 considered in all simulations. The correlations decrease noticeably with the size of  
524 the bucket at a given distance in both PARSIVEL<sup>2</sup> and 2DVD based simulations  
525 (Figure 9a-b). The decrease in correlations was gradual for disdrometer but quite  
526 sharp for coarser relation bucket size based simulations from nugget to short  
527 separation distances. At 2 km separation distance, the differences in correlations  
528 were approximately 0.2 between disdrometer and 0.254 mm bucket simulations of  
529 2DVD and PARSIVEL<sup>2</sup>.

530

## 531 8. Conclusions

532

533 The pixel-scale variability of seven DSD and eight integral rain parameters was  
534 investigated through a *unique* set of disdrometer observations where collocated  
535 2DVD and PARSIVEL<sup>2</sup> were operated at six sites across the main base of NASA/WFF.  
536 A three-parameter exponential function was employed to quantify the spatial  
537 variability. The  $r_0$ , or nugget parameter, was fixed to 0.99 and  $d_0$  and  $s_0$  were  
538 retrieved minimizing RMSE following fitting an exponential function to the  
539 correlations that were derived from 2DVD or PARSIVEL<sup>2</sup> observations. The  
540 correlations were calculated during periods when all twelve disdrometers reported

541 rainfall and a minimum RR threshold of  $0.1 \text{ mm h}^{-1}$  was satisfied with a minimum of  
542 10 drops occurring in one-minute.

543

544 The there parameter exponential function is a simple mathematical form that  
545 expresses the observed correlations well. It converged rapidly for almost all  
546 physical parameters where RMSE was mostly less than 0.08. Very good agreement  
547 between the 2DVD and PARSIVEL<sup>2</sup> derived correlations boosted our confidence in  
548 the quality of the observations. The 2DVD outperformed the PARSIVEL<sup>2</sup> for  
549 sampling of  $D_{\max}$ , while the reverse was true for  $N_T^*$ . This is likely due to the  
550 difference in the sensitivity of the respective disdrometers to the small and large  
551 drop end of the size spectrum.

552

553 Given the confidence in measurement quality and fitting method,  $d_0$  and  $s_0$  should  
554 mainly be sensitive to the characteristics of the DSD. The exclusion of a site did not  
555 change the distribution of rainfall resulting in insignificant changes in  $d_0$  and  $s_0$  of  
556 RR. The retrieved parameters of exponential function fits quite different in  
557 PARSIVEL<sup>2</sup> derived  $D_{\max}$  when one site was removed but this is attributed to the  
558 poor fitting. The  $d_0$  and  $s_0$  were sensitive to the different rain/no-rain thresholds.  
559 They were also sensitive to the differences in conditions where one or more and all  
560 six PARSIVEL<sup>2</sup> were reporting rainfall. The differences in the sample of  
561 observations play a key role for differences in  $d_0$  and  $s_0$ . The disdrometers have a  
562 clear advantage to the rain gauges when spatial variability was studied for short  
563 time intervals. The larger the bucket size the lower the correlations when the

564 disdrometer observations were used to simulate rain gauge observations at  
565 different bucket size.

566

567 This is the first study where the three-parameter exponential function has been  
568 used for estimating the variability of 15 physical parameters. Previously, JB12 used  
569 the exponential function for RR. Their study was more robust in terms of the  
570 number of available instruments and a longer period of observation. The  
571 correlations decreased more rapidly for the first 500 m reaching 0.8 in JB12 study.

572 This study did not have any paired correlation in this short distance regime and the  
573 correlation of RR was about 0.9 at 500 m. The differences in correlations are  
574 attributed to the nature of rain. JB12 study included higher rainfall intensities than  
575 this study.

576

577 The logistics often dominate the experiment set up and therefore the minimum and  
578 maximum distances in the study domain. The sample size and type of rainfall play a  
579 crucial role in quantifying the spatial variability. WFF is ideal site since rainfall from  
580 multiple weather systems falls in all around year. In this study, light rain was  
581 persistent throughout field study where mean RR was  $1.1 \text{ mm h}^{-1}$  and the 95<sup>th</sup>  
582 percentile of  $D_{\max}$  was 3.1 mm (2DVD). For future studies, the larger domain where  
583 the maximum disdrometer distance exceeds the DPR footprint and the combination  
584 of light and heavy rain is desirable for quantification of spatial variability of DSD.  
585 The limited but unique data set from Mid-latitude Continental Convective Clouds

586 experiment from Northern Oklahoma may prove to be a great resource for such a  
587 follow-up study.

588

589 Acknowledgements

590

591 The authors are grateful to the NASA Wallops Precipitation Facility team, Matthew  
592 Wingo, Katherine (Rhonie) Wolff, Paul G. Bashor, and Jason C. Bashor, for their  
593 efforts on maintaining the disdrometer network. Discussion with Robert Meneghini  
594 of NASA Goddard Space Flight Center (GSFC) was very helpful. This study was  
595 partly conducted during second authors' visit to the NASA GSFC. The funding for the  
596 second author's visit was provided through Federico Porcu of the University of  
597 Bologna, Italy. This study was funded through NASA Precipitation measurement  
598 mission grant NNX10AJ12G and funding from the Global Precipitation Measurement  
599 Mission.

600

601 References

602

603 Beard, K. V., 1976: Terminal velocity and shape of cloud and precipitation drops  
604 aloft. *J. Atmos. Sci.*, 33, 851-864.

605

606 Bringi, V. N., R. Rang, and V. Chandrasekar, 2004: Evaluation of a new  
607 polarimetrically based Z-R relation. *J. Atmos. Oceanic Technol.*, 21, 612-623.

608

609 Bringi, V., L. Tolstoy, M. Thurai, and W. Petersen, 2015: Estimation of spatial  
610 correlation of rain drop size distribution parameters and rain rate using NASA's S-  
611 band polarimetric radar and 2D-video disdrometer network: Two case studies from  
612 MC3E. *J. Hydrometeor.* doi:10.1175/JHM-D-14-0204.1, in press.

613

614 Ciach, G. J., and W. F. Krajewski, 2006: Analysis and modeling of spatial correlation  
615 structure of small-scale rainfall in Central Oklahoma. *Adv. Water Resour.*, 1450-  
616 1463.

617

618 D'Adderio, L. P., F. Porcu, and A. Tokay, 2015: Raindrop size distribution in the  
619 presence of break-up. *J. Atmos Sci.* (accepted for publication).

620

621 Gebremichael, M., and W. F. Krajewski, 2004: Characterization of the temporal  
622 sampling error in space-time-averaged rainfall estimates from satellite. *J. Geophys.*  
623 *Research.*, 109, doi: 10.1029/2004JD04509.

624

625 Habib, E., W. Krajewski, and A. Kruger, A., 2001: Sampling Errors of Tipping-Bucket  
626 Rain Gauge Measurements. *J. Hydrol. Eng.*, 6(2), 159–166.

627

628 Habib, E., and W. Krajewski, 2002: Uncertainty analysis of the TRMM ground-  
629 validation radar-rainfall products: Application to the TEFLUN-B field campaign. *J.*  
630 *Appl. Meteor.*, 41, 558-572.

631

- 632 Hou, A., R. Kakar, S. Neeck, A. A. Azarbarzin, C. D. Kummerow, M. Kojima, R. Oki, K.  
633 Nakamura, and T. Iguchi, 2014: The global precipitation measurement mission. Bull.  
634 Amer. Meteor. Soc., 95, 701-722.
- 635
- 636 Jaffrain, J., A. Studzinski, and A. Berne, 2011: A network of disdrometers to quantify  
637 the small-scale variability of the raindrop size distribution. Water Resources Resea.,  
638 47, W00H06, doi:10.1029/2010WR009872.
- 639
- 640 Jaffrain, J., and A. Berne, 2012: Quantification of the small-scale spatial structure o  
641 fthe raindrop size distribution from metwork of disdrometers. J. Applied Meteor.  
642 Climatol., 51, 941-953.
- 643
- 644 Moreau, E., J. tested, and E. Le Bouar, 2009: Rainfall special variability observed by  
645 X-band weather radar and its implication for the accuracy of rainfall estimates. Adv.  
646 Water Resour., 32, 1011-1019.
- 647
- 648 Schöenhuber, M., G. Lammer, and W. L. Randeu, 2007: One decade of imaging  
649 precipitation measurement by 2D video disdrometer. Adv. Geosci., 10, 85-90.
- 650
- 651 Schröer, J-B, 2011: Spatial and temporal variability of raindrop size distribution.  
652 Diploma Thesis. The University of Bonn, Bonn, Germany, 133pp.
- 653

- 654 Seto, S., T. Iguchi, and T. Oki, 2013: The basic performance of a precipitation  
655 retrieval algorithm for the global precipitation measurement mission's single/dual-  
656 frequency radar measurements. *IEEE Trans. Geoscience Rem. Sensing*, 51, 5239-  
657 5251.
- 658
- 659 Tapiador, F. J., R. Checa, and M. de Castro, 2010: An experiment to measure the  
660 spatial variability of raindrop size distribution using sixteen laser disdrometers.  
661 *Geophys. Res. Lett.*, 37, L16803, doi: 10.1029/2010GRL044120.
- 662
- 663 Thurai, M., W. A. Petersen, A. Tokay, C. Schultz, and P. Gatlin, 2011: Drop size  
664 distribution comparisons between PARASIVE and 2-D video disdrometers. *Adv.*  
665 *Geosci.*, 30, 3-9.
- 666
- 667 Tokay, A., A. Kruger, W. Krajewski, P. A., Kucera, and A. J. Pereira Filho, 2002:  
668 Measurements of drop size distribution in the southwestern Amazon basin. *J.*  
669 *Geophys. Res.*, **107**, D20, 8052, doi:10.1029.
- 670
- 671 Tokay, A., P. G. Bashor, and K. R. Wolff, 2005: Error characteristics of rainfall  
672 measurements by collocated Joss-Waldvogel disdrometers. *J. Atmos. Oceanic*  
673 *Technol.*, 22, 513-527.
- 674
- 675 Tokay, A., and P. G. Bashor, 2010: An experimental study of small-scale variability of  
676 raindrop size distribution. *J. Hydrometeorol.*, 11, 2348-2365.

- 677
- 678 Tokay, A., and K. Öztürk, 2012: An experimental study of the small-scale variability of  
679 rainfall. *J. Hydrometeor.*, 13, 351-365.
- 680
- 681 Tokay, A., W. A. Petersen, P. Gatlin, and M. Wing, 2013: Comparison of raindrop size  
682 distribution measurements by collocated disdrometers. *J. Atmos. Oceanic Technol.*,  
683 30, 1672-1690.
- 684
- 685 Tokay, A., R. J. Roche, and P. G. Bashor, 2014a: An experimental study of spatial  
686 variability of rainfall. *J. Hydrometeor.*, 15, 801-812.
- 687
- 688 Tokay, A., D. B. Wolff, and W. A. Petersen, 2014b: Evaluation of the new version of  
689 the laser-optical disdrometer, OTT PARSIVEL<sup>2</sup>. *J. Atmos. Oceanic Technol.*, 31, 1276-  
690 1288.
- 691
- 692 Villarini, G., P. V. Mandapaka, W. F. Krajewski, and R. J. Moore, 2008: Rainfall and  
693 sampling uncertainties: A rain gauge perspective. *J. Geophy. Resea.*, 113, doi:  
694 10.1029/2007/JD009214.
- 695
- 696 Williams, C. R., V. N. Bringi, L. D. Carey, V. Chandrasekar, P. N. Gatlin. Z. S. Haddad, R.  
697 Meneghini, S. J. Munchak, S. W. Nesbitt, W. A. Petersen, S. Tanelli, A. Tokay, A. Wilson,  
698 and D. B. Wolff, 2014: Describing the shape of raindrop size distributions using

699 uncorrelated raindrop mass spectrum parameters. J. Applied Meteor. Climatol., 53,

700 1282-1296.

701

702

703

704   Figure Captions:

705

706   Figure 1. Google Map of six field sites at the NASA Wallops Flight Facility (top).

707   Picture of 2DVD, PARSIVEL<sup>2</sup> among other precipitation measuring instruments at  
708   the Pad (middle) and at the Automated Surface Observing System site (bottom).

709   Please note that not all the instruments collecting data at the Pad during the  
710   experiment period.

711

712   Figure 2. Dependence of the correlation distance to correlation coefficient at a given  
713   distance and shape parameter when nugget parameter is set to 0.99. Four different  
714   shape parameters and two different distances are used.

715

716   Figure 3. Probability and cumulative distributions of (a) mass weighted diameter,  
717   (b) maximum diameter, (c) logarithmic normalized intercept parameter,  $N_T^*$ , (d)  
718   logarithmic normalized intercept parameter,  $N_w$ , (e) shape parameter with respect  
719   to  $N_T^*$ , (f) shape parameter with respect to  $N_w$ , (g) shape parameter with respect to  
720    $\sigma_{\text{mass}}$ , (h) liquid water content, (i) rain rate, (j) horizontal reflectivity, (k) differential  
721   reflectivity, (l) reflectivity at W-band, (m) reflectivity at Ku-band, (n) reflectivity at  
722   Ka-band, (o) dual frequency ratio. Distributions of these physical parameters are  
723   derived from 2DVD and PARSIVEL<sup>2</sup> observations.

724

725   Figure 4. Spatial variability of (a) mass weighted diameter, (b) maximum diameter,  
726   (c) logarithmic normalized intercept parameter,  $N_T^*$ , (d) logarithmic normalized

727 intercept parameter,  $N_w$ , (e) shape parameter with respect to  $N_T^*$ , (f) shape  
728 parameter with respect to  $N_w$ , (g) shape parameter with respect to  $\sigma_{\text{mass}}$ , (h) liquid  
729 water content, (i) rain rate, (j) horizontal reflectivity, (k) differential reflectivity, (l)  
730 reflectivity at W-band, (m) reflectivity at Ku-band, (n) reflectivity at Ka-band, (o)  
731 dual frequency ratio, all derived from 2DVD (blue dots) and PARSIVEL<sup>2</sup> (red stars)  
732 observations. The parameters of the three-parameter exponential function  
733 including root-mean-square error and the sample size are also given.

734

735 Figure 5. (a) Correlation distance and (b) shape parameter of the three-parameter  
736 exponential function and (c) root-mean-square error for fifteen physical parameters  
737 based on 2DVD (blue dots) and PARSIVEL<sup>2</sup> (red stars) observations. Several  
738 correlation distances were higher than y-axis range and are marked with their  
739 values.

740

741 Figure 6. Sensitivity of (a) the correlation distance, (b) shape parameter of the  
742 three-parameter exponential function and of (c) root-mean-square error of mass  
743 weighted diameter (left) and rain rate (right) to the elimination of a site (e.g. site1)  
744 during the experiment. Several correlation distances were higher than y-axis range  
745 and are marked with their values.

746

747 Figure 7. Sensitivity of (a) the correlation distance, (b) shape parameter of the  
748 three-parameter exponential function and of (c) root-mean-square error of fifteen  
749 physical parameters to the rainfall threshold following 2DVD observations. The

750 rainfall thresholds of  $Z_{\text{Ka}} > 12$  dB (green dot),  $Z_{\text{Ku}} > 18$  dB (black dot), and  $\text{RR} > 0.1 \text{ m}$   
751  $\text{h}^{-1}$  (red dot) are considered. Several correlation distances were higher than y-axis  
752 range and are marked with their values.

753

754 Figure 8. Sensitivity of (a) the correlation distance, (b) shape parameter of the  
755 three-parameter exponential function and of (c) root-mean-square error of fifteen  
756 physical parameters to rain coverage. One or more (orange stars) as well as all six  
757 (red stars) PARSIVEL<sup>2</sup> reporting rainfall was considered. Several correlation  
758 distances were higher than y-axis range and are marked with their values.

759

760 Figure 9. Spatial variability of 5-minute rainfall derived from (a) 2DVD and (b)  
761 PARSIVEL<sup>2</sup> observations (red), simulated gauge at 0.1 mm bucket (blue), simulated  
762 gauge at 0.2 mm bucket (green), and simulated gauge at 0.254 mm bucket (black).

763

764

765 Table 1. NASA Wallops Flight Facility Precipitation Data Acquisition Network. The  
766 distances between the six sites are given in km.

767

	Site #	Site 1	Site 2	Site 3	Site 4	Site 5	Site 6
	Site name	Pad	ASOS	Balloon Launch Facility	Building A41	Visitor Center	Water Treatment Plant
	Coord inates	37.944°N, 75.464°W	37.944°N, 75.481°W	37.938°N, 75.456°W	37.934°N, 75.471°W	37.929°N, 75.473°W	37.937°N, 75.466°W
Site 1			0.51	0.60	1.25	1.34	1.41
Site 2				1.06	1.81	0.88	1.53
Site 3					1.84	1.75	1.80
Site 4						0.99	1.52
Site 5							2.31

768

769

770 Table 2: Mean, standard deviation, median, and 5th and 95th percentiles of seven  
 771 DSD and eight integral parameters that were derived from 2DVD and PARSIVEL<sup>2</sup>  
 772 (Par<sup>2</sup>) observations.  
 773

DSD and integral rain parameters	mean		standard deviation		median		5 <sup>th</sup> percentile		95 <sup>th</sup> percentile	
	2DVD	Par <sup>2</sup>	2DVD	Par <sup>2</sup>	2DVD	Par <sup>2</sup>	2DVD	Par <sup>2</sup>	2DVD	Par <sup>2</sup>
D <sub>mass</sub> (mm)	1.11	1.09	0.30	0.32	1.05	1.01	0.72	0.72	1.64	1.63
D <sub>max</sub> (mm)	2.03	1.96	0.58	0.63	1.92	1.93	1.28	1.22	3.07	3.35
N <sub>T</sub> * (m <sup>-3</sup> mm <sup>-1</sup> )	302	951	394	2,271	184	319	47	64	1,065	4,274
N <sub>w</sub> (m <sup>-3</sup> mm <sup>-1</sup> )	6,524	7,313	9,294	10,915	3,468	3,588	711	53	26,787	32,706
m(N <sub>T</sub> *)	4.85	5.95	2.92	3.87	4.40	5.10	1.10	1.40	10.30	13.65
m(N <sub>w</sub> )	5.16	5.00	3.38	4.01	4.50	4.00	0.80	0.10	11.40	12.90
m(σ <sub>mass</sub> )	5.75	5.41	3.54	4.18	5.23	4.60	0.90	-0.01	12.14	13.45
RR (mmh <sup>-1</sup> )	1.10	1.15	0.94	1.00	0.87	0.91	0.25	0.27	2.94	2.92
W (gm <sup>-3</sup> )	0.071	0.077	0.054	0.056	0.059	0.065	0.019	0.021	0.188	0.191
Z <sub>h</sub> (dB)	26.4	27.7	18.0	33.4	22.3	22.1	15.0	15.0	31.2	31.8
Z <sub>dr</sub> (dB)	0.376	0.394	0.291	0.427	0.287	0.273	0.119	0.112	0.839	0.938
Z <sub>W</sub> (dB)	16.9	17.3	3.4	3.2	15.8	16.4	11.3	11.8	20.8	21.1
Z <sub>Ku</sub> (dB)	26.8	27.7	18.5	22.1	21.9	21.7	14.8	14.7	31.7	32.7
Z <sub>Ka</sub> (dB)	26.3	26.2	5.8	6.3	23.4	23.2	15.2	15.5	31.4	31.5
DFR	-0.99	-0.86	1.19	1.11	-1.27	-1.04	-2.04	-1.86	1.26	0.78

774

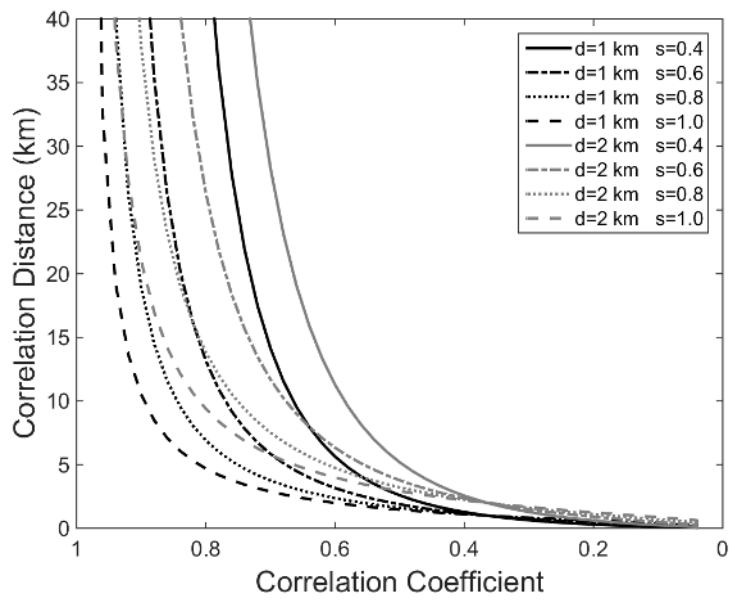
775

776



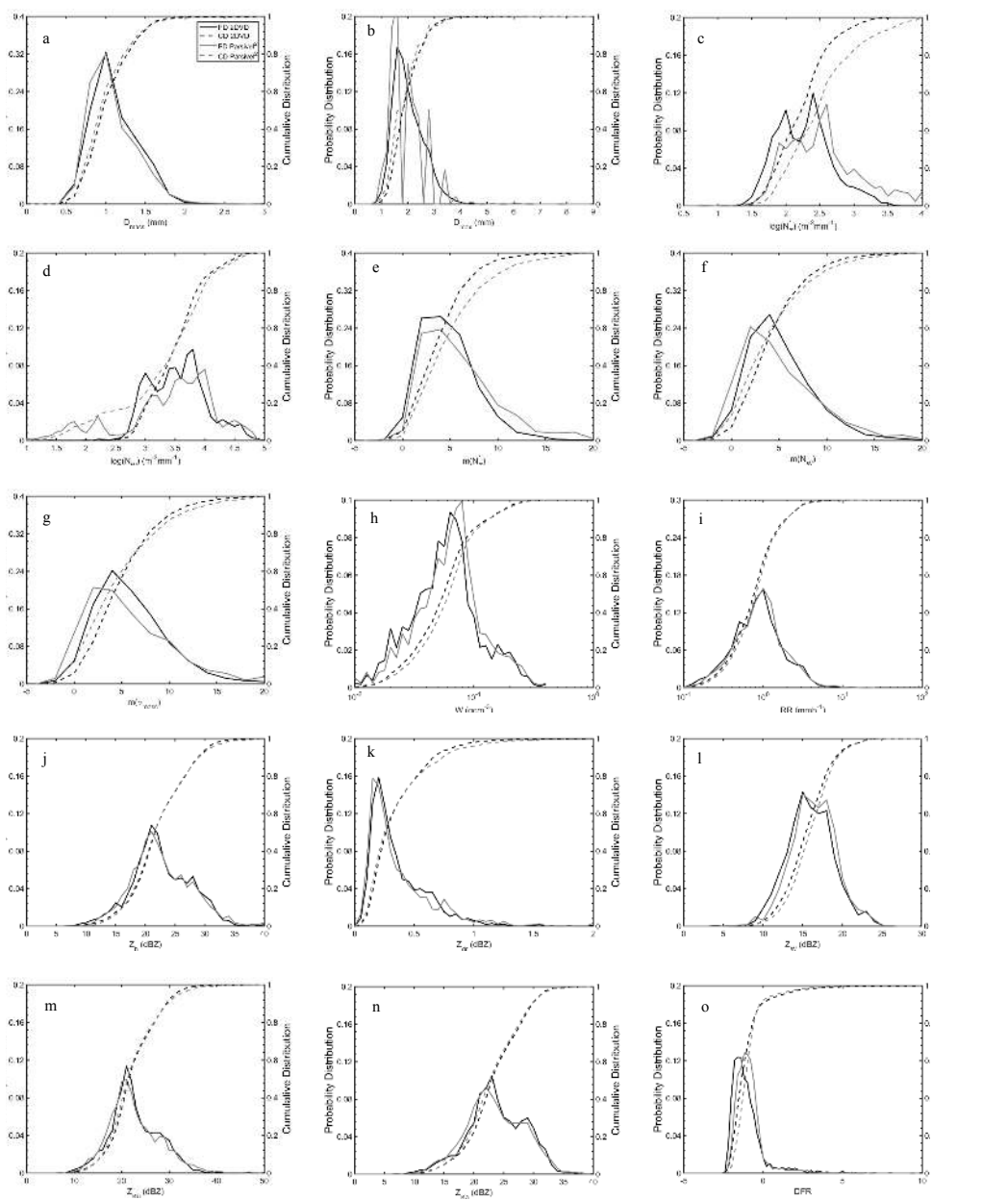
777

778 Figure 1. Google Map of six field sites at the NASA Wallops Flight Facility (top).  
779 Picture of 2DVD, PARSELV<sup>2</sup> among other precipitation measuring instruments at  
780 the Pad (middle) and at the Automated Surface Observing System site (bottom).  
781 Please note that not all the instruments collecting data at the Pad during the  
782 experiment period.  
783  
784



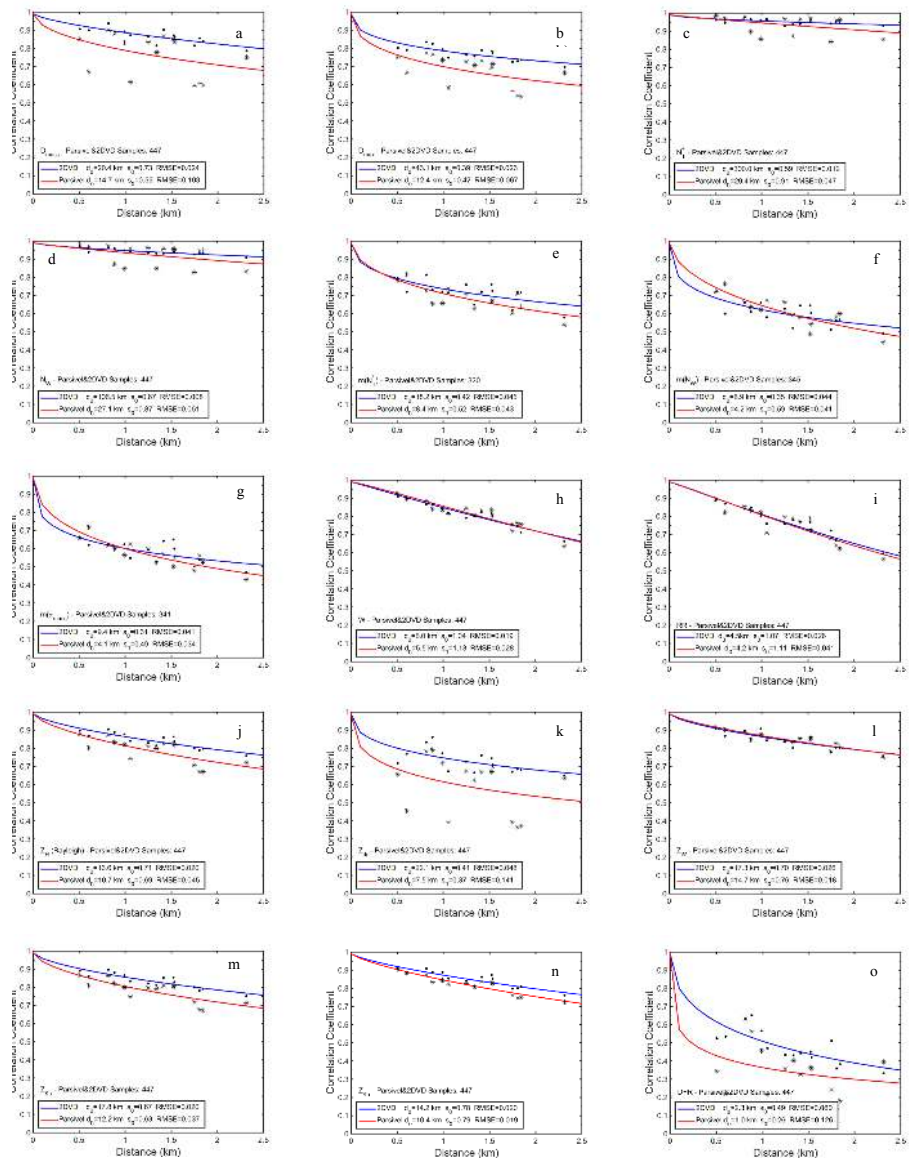
785  
 786  
 787  
 788  
 789  
 790  
 791  
 792

Figure 2. Dependence of the correlation distance to correlation coefficient at a given distance and shape parameter when nugget parameter is set to 0.99. Four different shape parameters and two different distances are used.



793  
794  
795  
796  
797  
798  
799  
800  
801

Figure 3. Probability and cumulative distributions of (a) mass weighted diameter, (b) maximum diameter, (c) logarithmic normalized intercept parameter,  $N_T^*$ , (d) logarithmic normalized intercept parameter,  $N_w$ , (e) shape parameter with respect to  $N_T^*$ , (f) shape parameter with respect to  $N_w$ , (g) shape parameter with respect to  $\sigma_{\text{mass}}$ , (h) liquid water content, (i) rain rate, (j) horizontal reflectivity, (k) differential reflectivity, (l) reflectivity at W-band, (m) reflectivity at Ku-band, (n) reflectivity at Ka-band, (o) dual frequency ratio. Distributions of these physical parameters are derived from 2DVD and PARSIVEL<sup>2</sup> observations.



802

803

804

805

806

807

808

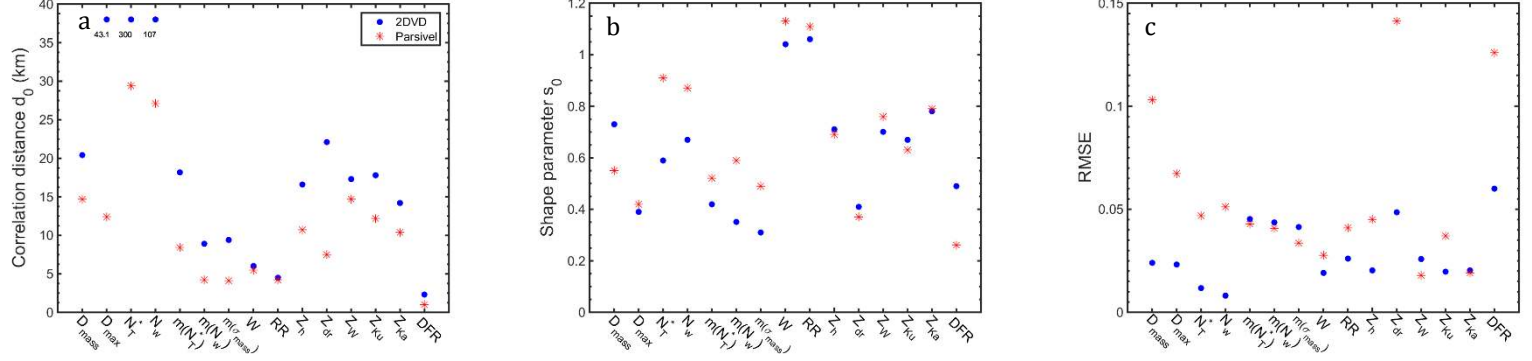
809

810

811

812

Figure 4. Spatial variability of (a) mass weighted diameter, (b) maximum diameter, (c) logarithmic normalized intercept parameter,  $N_T^*$ , (d) logarithmic normalized intercept parameter,  $N_w$ , (e) shape parameter with respect to  $N_T^*$ , (f) shape parameter with respect to  $N_w$ , (g) shape parameter with respect to  $s_{\text{mass}}$ , (h) liquid water content, (i) rain rate, (j) horizontal reflectivity, (k) differential reflectivity, (l) reflectivity at W-band, (m) reflectivity at Ku-band, (n) reflectivity at Ka-band, (o) dual frequency ratio, all derived from 2DVD (blue dots) and PARSIVEL<sup>2</sup> (red stars) observations. The parameters of the three-parameter exponential function including root-mean-square error and the sample size are also given.



813

814 Figure 5. (a) Correlation distance and (b) shape parameter of the three-parameter  
 815 exponential function and (c) root-mean-square error for fifteen physical parameters  
 816 based on 2DVD (blue dots) and PARSIVEL<sup>2</sup> (red stars) observations. Several  
 817 correlation distances were higher than y-axis range and are marked with their  
 818 values.

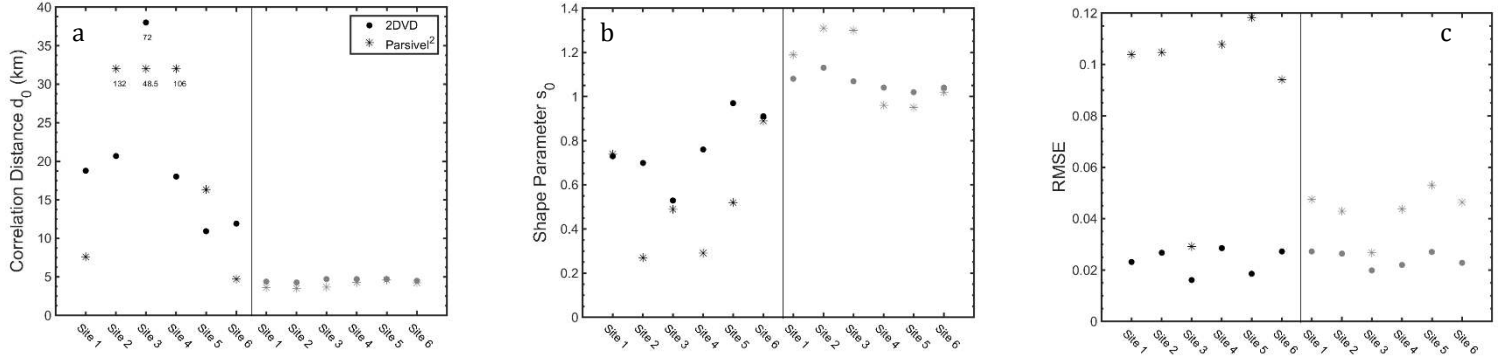
819

820

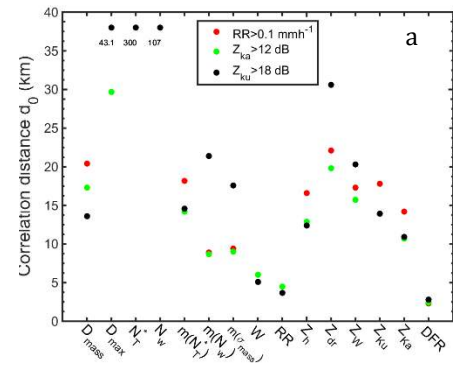
821

822

823  
824  
825



826  
827 Figure 6. Sensitivity of (a) the correlation distance, (b) shape parameter of the  
828 three-parameter exponential function and of (c) root-mean-square error of mass  
829 weighted diameter (left) and rain rate (right) to the elimination of a site (e.g. site1)  
830 during the experiment. Several correlation distances were higher than y-axis range  
831 and are marked with their values.  
832  
833  
834  
835



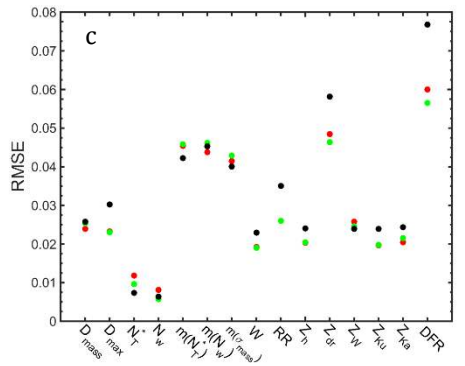
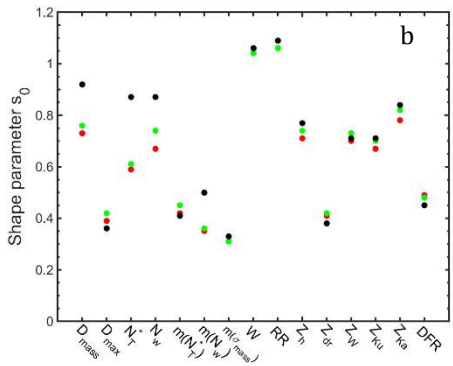
836

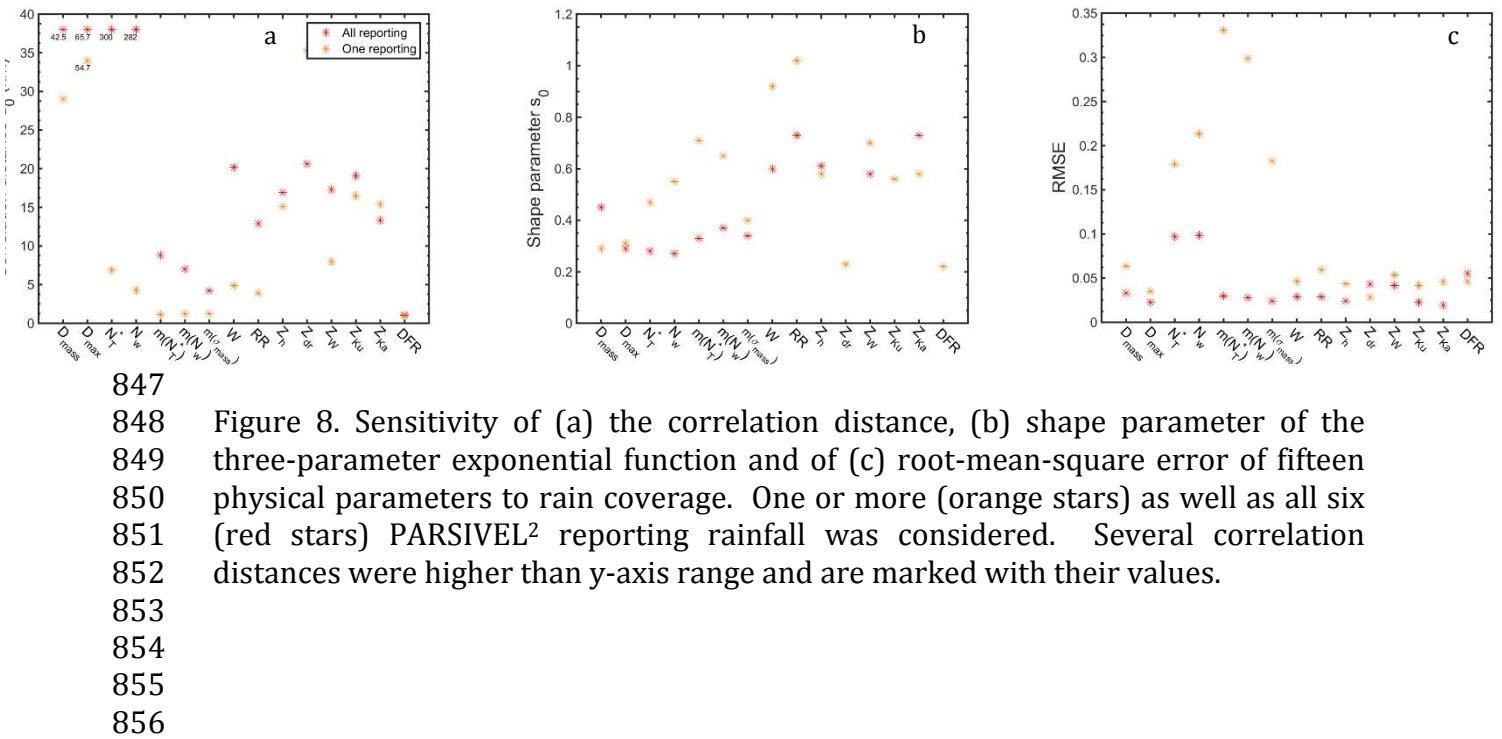
837 Figure 7. Sensitivity of (a) the correlation distance, (b) shape parameter of the  
 838 three-parameter exponential function and of (c) root-mean-square error of fifteen  
 839 physical parameters to the rainfall threshold following 2DVD observations. The  
 840 rainfall thresholds of  $Z_{Ka} > 12$  dB (green dot),  $Z_{Ku} > 18$  dB (black dot), and  $RR > 0.1$  m  
 841  $h^{-1}$  (red dot) are considered. Several correlation distances were higher than y-axis  
 842 range and are marked with their values.

843

844

845





847

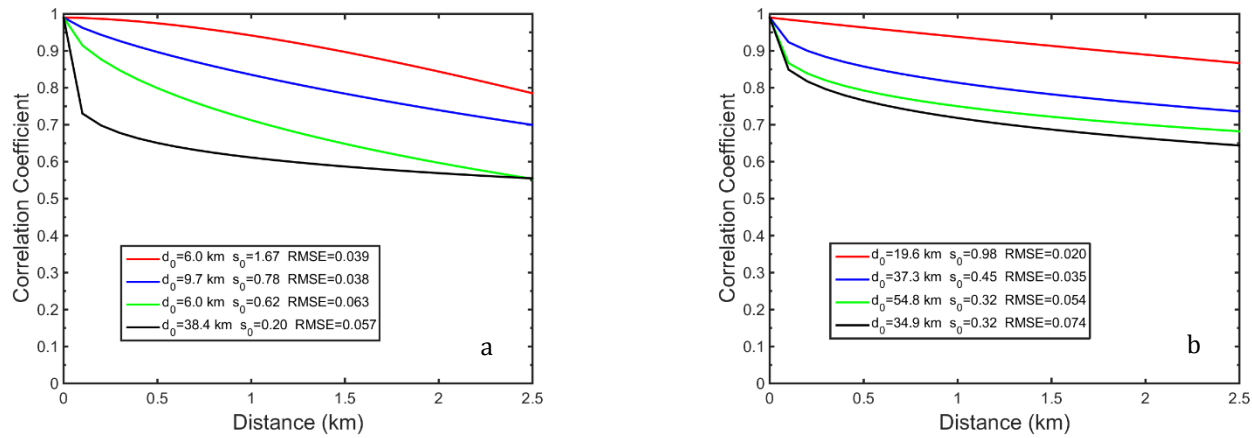
848 Figure 8. Sensitivity of (a) the correlation distance, (b) shape parameter of the  
 849 three-parameter exponential function and of (c) root-mean-square error of fifteen  
 850 physical parameters to rain coverage. One or more (orange stars) as well as all six  
 851 (red stars) PARSIVEL<sup>2</sup> reporting rainfall was considered. Several correlation  
 852 distances were higher than y-axis range and are marked with their values.

853

854

855

856



859     Figure 9. Spatial variability of 5-minute rainfall derived from (a) 2DVD and (b)  
860     PARSIVEL<sup>2</sup> observations (red), simulated gauge at 0.1 mm bucket (blue), simulated  
861     gauge at 0.2 mm bucket (green), and simulated gauge at 0.254 mm bucket (black).